1 # U-Pb monazite ages of the Kabanga mafic-ultramafic

2 # intrusions and contact aureoles, central Africa:

3 # geochronological and tectonic implications

4

5 Jian-Wei Zi[1,2*], Birger Rasmussen[1,3], Janet R. Muhling[3], Wolfgang D. Maier[4],

6 Ian R. Fletcher[2]

7

8 [1] State Key Lab of Geological Processes and Mineral Resources, China

9 University of Geosciences, Wuhan 430074, China

10 [2] John de Laeter Centre, Curtin University, Kent Street, Bentley, WA 6102,

11 Australia

12 [3] School of Earth Sciences, The University of Western Australia, Stirling

13 Highway, Perth, WA 6009, Australia

14 [4] School of Earth and Ocean Sciences, Cardiff University, Park Place, Cardiff

15 CF10 3AT, UK

16

17 *corresponding author (zijw@hotmail.com)

18 **ABSTRACT**

19   Mafic-ultramafic rocks of the Kabanga-Musongati (KM) alignment in the

20 East African Nickel Belt occur as Bushveld-type layered intrusions emplaced

21 in metasedimentary sequences. The age of the mafic-ultramafic intrusions

22 remains poorly constrained, though they are regarded to be part of ca. 1375

23 Ma bimodal magmatism dominated by voluminous S-type granites. In this

24 study, we investigate igneous monazite and zircon from a differentiated

25 layered intrusion and metamorphic monazite from the contact aureole. The

26 monazite shows contrasting crystal morphology, chemical composition and U-

27 Pb age. Monazite formed by contact metamorphism in response to

28 emplacement of mafic-ultramafic melts is characterized by extremely high Th

29 and U, and yielded a weighted mean $^{207}Pb/^{206}Pb$ age of 1402 ± 9 Ma, which is

30 in agreement with dates from the igneous monazite and zircon. The ages

31 indicate that the intrusion of ultramafic melts was substantially earlier (by

32 approximately 25 million years, 95% confidence) than the prevailing S-type

33 granites, calling for a reappraisal of the previously suggested model of coeval,

34 bimodal magmatism. Monazite in the metapelitic rocks also records two

35 younger growth events at ca. 1375 Ma and ca. 990 Ma, coeval with

36 metamorphism during emplacement of S-type granites and tin-bearing

37 granites, respectively. In conjunction with available geologic evidence, we

38 propose that the KM mafic-ultramafic intrusions likely heralded a structurally

39 controlled thermal anomaly related to Nuna breakup, which culminated during

40 the ca. 1375 Ma Kibaran event manifested as extensive intracrustal melting in

41 the adjoining Karagwe-Ankole Belt (KAB), producing voluminous S-type

42 granites. The Grenvillian-aged (ca. 990 Ma) tin-bearing granite and related Sn

43 mineralization appear to be the far-field record of tectonothermal events

44 associated with collision along the Irumide Belt during Rodinia assembly.

45 Since monazite is a ubiquitous trace phase in pelitic sedimentary rocks in

46 contact aureoles of mafic-ultramafic intrusions or in regional metamorphic

47 belts, our study highlights the potential of using metamorphic monazite to

48 determine ages of mafic-ultramafic intrusions, and to reconstruct post-

49 emplacement metamorphic history of the host terranes.

50

51 **Key words:** U-Pb monazite geochronology; Mafic-ultramafic intrusions;

52 Karagwe-Ankole Belt; Kabanga; Nuna breakup; Rodinia assembly

53

54 **INTRODUCTION**

55   Mafic-ultramafic intrusions emplaced in continental terranes indicate

56 regional lithospheric extension, and are typically associated with continental

57 rifting and/or mantle plume activity (Ernst and Buchan, 2001). As such, mafic

58 intrusions (e.g., mafic dike swarms) have played a crucial role in tracing

59 plume-generated large igneous provinces and reconstructing ancient

60 supercontinents (Ernst et al., 2013; Evans, 2013). Mafic-ultramafic intrusive

61 bodies may also be repositories of a variety of base and precious metals (e.g.,

62 Ni, Cu, PGEs) that are of significant economic importance (Arndt et al., 2003;

63 Begg et al., 2010). However, obtaining accurate and precise ages from mafic-

64 ultramafic rocks has proven to be challenging due to the scarcity within them

65 of U-bearing accessory minerals suitable for successful dating. Where present,

66 baddeleyite and/or zircon can be used in direct dating of mafic intrusive rocks

67 (Hulbert et al., 2005; Heaman, 2009; Chamberlain et al., 2010; Scoates et al.,

2017), but the technique often confronts complications due to the presence of xenocrysts, crustal contamination and metamorphic overprint (Black et al., 1991; Heaman and LeCheminant, 1993; Maier et al., 2015). In many cases, it is exceedingly difficult to assemble an adequate number of crystals for analysis because of their extremely low quantities and small crystal size. Another U-bearing zirconium phase, zirconolite, has been shown to be a robust chronometer that can be used to date mafic rocks (Rasmussen and Fletcher, 2004; Rasmussen et al., 2009), yet the usefulness of this technique is limited by the restricted occurrence of the mineral and post-crystallization alteration. Other techniques such as Ar-Ar, Sm-Nd, and Rb-Sr are considered less reliable due to their susceptibility to later thermal resetting, a problem particularly acute for Precambrian rocks that have typically endured extensive alteration.

Intrusion of mafic-ultramafic rocks commonly induces contact metamorphism and/or partial melting of country rocks which may lead to new growth of U-bearing minerals (e.g., zircon and monazite), bestowing a useful 'indirect' approach for determining the timing of emplacement of the intrusions. In a study of Proterozoic mafic-ultramafic intrusions in the Sveconorwegian Province, SW Sweden, Scherstén et al. (2000) derived ages of the intrusions by analyzing newly crystallized zircon grains and overgrowths on xenocrysts in the country rocks. This indirect dating approach has been advanced through investigation of other mineral phases such as monazite. As a versatile chronometer, monazite is well-known for its capability of recording a wide range of geological processes from granitic magmatism and high-grade metamorphism to low-grade hydrothermal infiltration and related

93   mineralization (Parrish, 1990; Williams et al., 2007), because it is susceptible

94   to dissolution-reprecipitation induced by tectonic and thermal events over

95   prolonged periods (Williams, 2001; Rasmussen and Muhling, 2007; Harlov et

96   al., 2011; Williams et al., 2011; Seydoux-Guillaume et al., 2012). By dating

97   metamorphic monazite crystals within a contact aureole, U-Pb ages that

98   correspond to the timing of magma emplacement can be obtained. This

99   approach has proven to be applicable to determining ages of intrusions of

100   various types such as mafic intrusions (Rasmussen and Fletcher, 2002),

101   granite plutons (Rasmussen et al., 2001; Ayers et al., 2013) and an alkaline-

102   carbonatite complex (Zi et al., 2017).

103   In this paper, we further explore the potential of monazite in revealing

104   the intricate history of igneous intrusions particularly in areas that have

105   experienced multiple magmatic-metamorphic events. The Kabanga-

106   Musongati alignment in Tanzania and Burundi is ideal for such a study

107   because it is characterized by mafic-ultramafic intrusions and granite plutons

108   emplaced into sedimentary rocks. Existing geochronological data in the region

109   indicate a predominant episode of igneous activity at ca. 1375 Ma, interpreted

110   to be a single bimodal magmatism marking the Kibaran event (Tack et al.,

111   2010). However, the age constraints are mainly from granitoids, and there is

112   evidence that the mafic-ultramafic layered intrusions, which host world-class

113   nickel sulfide deposits, must have predated the granites (Evans et al., 1999;

114   Maier et al., 2007; Maier et al., 2010). In this study, we mainly target monazite

115   in the sedimentary rocks that have been affected by contact metamorphism in

116   response to igneous intrusions, and establish a precise record of the history of

117   metamorphic monazite growth, which offers new insights into the timing and

118 geodynamic context of the igneous intrusions and related Ni-PGE

119 mineralization. The geochronology data reported in this contribution,

120 integrated with available geologic evidence, allows recognition of multiple

121 episodes of igneous/metamorphic events which are readily correlated with

122 contemporaneous global-scale magmatism in the context of tectonic transition

123 from Nuna to Rodinia configuration.

124

125 **GEOLOGICAL BACKGROUND**

126 **Geological setting**

127 Largely based on geophysical imagery, basin stratigraphy and

128 provenance analysis (Tack et al., 2010; Fernandez-Alonso et al., 2012), the

129 NE-trending, >1000 km long orogenic belt between the Congo and Tanzania

130 cratons has recently been subdivided into two segments, namely the

131 Karagwe-Ankole Belt (KAB) in the NE and the Kibaran Belt (KIB) in the SW,

132 separated by the NW-trending Paleoproterozoic Ubende-Rusizi belt (Fig. 1).

133 The KAB comprises two structurally contrasting domains: the Western

134 Domain (WD) and the Eastern Domain (ED), bounded by the NE-SW trending

135 Kabanga-Musongati (KM) alignment (Fig. 1).

136 The KM alignment is characterized by a series of mafic-ultramafic

137 intrusions emplaced in thick metasedimentary rocks. The southwestern

138 continuation of the mafic-ultramafic intrusions is truncated by Lake

139 Tanganyika, a possible western arm of the East African Rift Valley (Evans et

140 al., 2016), whereas the Kapalagulu intrusion, located on the eastern shore of

141 Lake Tanganyika (Fig. 1), is considered a southern extension of the KM

142 intrusions (Maier et al., 2008). The mafic-ultramafic intrusions of the KM

143 alignment host large nickel deposits and form the major components of the

144 East African Nickel Belt (Evans et al., 2016), which is also known as the

145 Central African Nickel Belt (Wilhelmij and Cabri, 2016).

146   Within the KM alignment and its vicinity, well-differentiated, Bushveld-

147 type layered intrusions are accompanied by small chonoliths, as well as

148 poorly differentiated, gabbronorite dykes and sills (Fig. 1). The layered mafic-

149 ultramafic intrusions are composed of dunite, peridotite, pyroxenite,

150 gabbronorite and anorthosite, showing magmatic layering and cumulate

151 textures, and contact metamorphic aureoles in the host rocks (Deblond and

152 Tack, 1999; Duchesne et al., 2004; Maier et al., 2008). The intrusions are

153 thought to have crystallized from a mantle-derived, high-Mg picritic or basaltic

154 magma, with various amounts of crustal assimilation (Evans et al., 1999;

155 Duchesne et al., 2004; Maier et al., 2008), though Duchesne et al. (2004) also

156 invoked a sub-continental lithospheric mantle source to explain the enriched

157 Nd isotopic signatures (ε_{Nd}(t) values of -8 to -3) observed in some

158 gabbronorite intrusions. The intrusions contain abundant sulfides, pyrrhotite,

159 pentlandite, and lesser amounts of chalcopyrite and pyrite (Evans et al., 1999;

160 Maier et al., 2010), forming the significant nickel sulfide deposits of the East

161 African Nickel Belt. The Kapalagulu intrusion also contains high-grade

162 platinum-group-element (PGE) mineralization associated with chromitite and

163 sulfide-bearing harzburgite (Maier et al., 2008; Wilhelmij and Cabri, 2016).

164   The mafic-ultramafic intrusions were emplaced within metasedimentary

165 rocks of the Karagwe-Ankole sedimentary sequences that unconformably rest

166 on the Archean-early Proterozoic basement of the Congo and Tanzania

167 cratons (Maier et al., 2010). The sedimentary sequences are composed of

168 thick successions (up to 5000 m) of alternating arenaceous and pelitic rocks

169 (Maier et al., 2010; Tack et al., 2010).

170   S-type granites are widespread in areas NW of the KM alignment (Fig.

171 1). Aeromagnetic anomalies have revealed a series of dolerite dykes

172 emplaced in Archean basement of the NW Tanzania craton and in the

173 Paleoproterozoic Buganda-Toro sequences of SW Uganda, forming the giant,

174 arcuate Lake Victoria dike swarm (Fig. 1). An enriched sub-continental

175 lithospheric mantle source has been proposed for the dike swarm based on

176 geochemical signatures (Mäkitie et al., 2014).

177   The mafic-ultramafic intrusions appear to have been emplaced prior to

178 the peak stage of the Kibaran event and associated syn-kinematic S-type

179 granitic plutonism (Evans et al., 1999; Evans et al., 2000; Maier et al., 2010),

180 and have been deformed during the latter event. Similar field relationships

181 have been documented by Kokonyangi et al. (2005) in the KIB where mafic

182 intrusions were thermally affected by the emplacement of granites leading to

183 growth of metamorphic mineral assemblage.

184

185 **Igneous history: existing geochronological constraints**

186   Maier et al. (2007) derived U-Pb zircon ages of 1403 ± 14 Ma for the

187 Kabanga North intrusion, and 1392 ± 26 Ma for the Kapalagulu intrusion. Tack

188 et al. (2010) reported U-Pb zircon geochronology results for an amphibole-

189 norite from Musongati, but the majority of the analyses are normally or

190 reversely discordant, which is ascribed to the combined effects of recent

191 and/or ancient Pb loss and radiation damage caused by high U contents. The

192 most concordant data (within ± 5% discordance) display high dispersion with

ages ranging from 1393 ± 12 Ma (1σ) to 1148 ± 50 Ma (1σ), and an older cluster giving a weighted mean $^{207}Pb/^{206}Pb$ age of 1374 ± 14 Ma (Tack et al., 2010). Hornblende from the same sample records a $^{40}Ar/^{39}Ar$ age of 1365 ± 2 Ma (Tack et al., 2010). In view of the effect of Pb loss in zircon (as illustrated by the high dispersion) and later thermal overprinting, it is likely that the $^{207}Pb/^{206}Pb$ zircon age represents a minimum estimate for the age of igneous crystallization of the rock, whereas the $^{40}Ar/^{39}Ar$ hornblende age may reflect cooling or resetting.

S-type granites from multiple plutons in Burundi and Rwanda yielded zircon ages indistinguishable within analytical uncertainties defining a narrow interval between 1380 Ma and 1370 Ma (Tack et al., 2010). S-type granites and mafic-ultramafic intrusions of similar age have been documented by Kokonyangi et al. (2005) in the KIB (Mitwaba area of the Democratic Republic of Congo), to the SW of the KM alignment. Later igneous activities, including emplacement of A-type granites (Bukirasazi massif, Burundi) at 1207 ± 11 Ma and tin-bearing granites (Kasika massif, DRC) at 986 ± 10 Ma, have been recorded and interpreted as representing minor magmatic additions to the crust (Tack et al., 2010). In the Mitwaba area, Kokonyangi et al. (2004, 2006) have also documented emplacement of tin-bearing granites dated at approximately 1000-950 Ma.

Two dikes of the Lake Victoria dike swarm from SW Uganda provide Sm-Nd isochron ages of 1368 ± 46 Ma and 1374 ± 42 Ma (Mäkitie et al., 2014). The similarity in age led Mäkitie et al. (2014) to suggest that the dike swarm and the ca. 1375 Ma "bimodal" magmatic rocks form a large igneous province related to the break-up of the Nuna supercontinent.

KABANGA LOCAL GEOLOGY AND SAMPLES

Local geology at Kabanga and in the adjoining areas, as well as the morphology and lithological correlation of the Kabanga mafic-ultramafic intrusions, have been described in detail in the literature (Evans et al., 1999; Evans et al., 2000; Maier et al., 2008; Maier et al., 2010; Evans et al., 2016).

A quartzite unit, with a thickness of up to 500 m, occurs as a distinct marker horizon in the footwall of the mafic-ultramafic intrusions at Kabanga (Fig. 2) (Evans et al., 2000; Maier et al., 2010). The quartzite is overlain by andalusite-muscovite-staurolite-biotite schists that locally contain garnet, suggesting a mid-amphibolite facies, high-T/low-P, regional metamorphism (Evans et al., 2000; Maier et al., 2010). Contact metamorphism in the thermal aureoles of the mafic-ultramafic intrusions reached the sillimanite and cordierite-K feldspar facies (Evans et al., 2000) forming narrow, light-colored hornfel zones a few meters in width (Fig. 3A; Maier et al., 2010). Fine-grained, relatively sulfide-poor, banded pelite (Fig. 3C) occurs as discontinuous, 25-75 m thick lenses within the mica schists (Maier et al., 2010).

The intrusions that contain the Kabanga nickel deposit are hosted within steeply-dipping to overturned metasedimentary rocks, and are adjacent to the Bushubi Granite (Fig. 2), which is composed of foliated S-type granite. This granite and its equivalents in the adjacent areas are related to the peak stage of the ca. 1375 Ma Kibaran event (Kokonyangi et al., 2004; Kokonyangi et al., 2005; Buchwaldt et al., 2008; Tack et al., 2010). The sedimentary sequence is made up predominantly of metapelites and metasiltstones (shales and schists), within minor arenitic metasandstones (quartzites). The

metapelite rocks are graphitic in places and can contain up to 5 modal % of pyrrhotite as thin layer-parallel laminae and lenses. They are schistose to phyllitic, with the metamorphic fabric dipping steeply to the WNW. The metamorphic grade decreases from amphibolite facies adjacent to the granite, to lower greenschist facies farther away to the east (Evans et al., 2016).

Despite intense weathering and thrusting of the sedimentary sequence at surface, the host rocks immediate to the Kabanga intrusions have been intersected in several deep drill-holes (Fig. 2; Evans et al., 2000; Maier et al., 2010). A total of five metasedimentary samples in the vicinity of the layered intrusions at Kabanga and Nyanzali were selected in this study, including muscovite schist samples K89 (drill-hole NYZD 002, drill-depth 193.1 m), K96 (KN 01-01B, 1356.15 m), K99 (KSM 06, 68.86 m) and K100 (KSM 06, 125.4 m), and a banded pelite sample K101 (KSM 04, 150.4 m). Also included is a pegmatoidal gabbronorite sample WM5 from Kabanga Main (drill-hole KN95-78, drill-depth 211.1 m), which forms a component of the layered intrusions, and comprises up to about 1 cm long pyroxene crystals in a dark matrix of primarily plagioclase and pyroxene.

ANALYTICAL METHOD

In situ U-Pb dating was conducted on monazite and zircon in the selected rock samples from Kabanga using the Sensitive High-Resolution Ion MicroProbe (SHRIMP II) housed at the John de Laeter Centre, Curtin University. Monazite analytical procedures are described and discussed in detail by Fletcher et al. (2010), and outlined in the Supplementary Information. Monazite reference standards (French, Z2908, Z2234, QMa28-1, PD-95)

268 were in a separate mount that was cleaned and Au-coated with the sample

269 mounts for each analytical session. SHRIMP operational settings and

270 calibration parameters are summarized in Table S1. Zircon analytical

271 procedures are similar to those applied by Rasmussen and Fletcher (2010) for

272 *in situ* analysis of small grains. Fragments of the calibration reference zircon

273 CZ3 were set in a 3-mm-diameter polished disc cast into the zircon sample

274 mount.

275   SHRIMP U-Pb data were reduced with Squid-2 software (Ludwig, 2009)

276 using spot average values for all ratios. A conventional exponential calibration

277 procedure (exp. = 2.0) was used for $^{206}Pb/^{238}U$ in zircon, and 1-D calibrations

278 of $^{206}Pb^+/^{270}[UO_2]^+$ and $^{208}Pb^+/^{264}[ThO_2]^+$ were used for monazite $^{206}Pb/^{238}U$

279 and $^{208}Pb/^{232}Th$, respectively (Fletcher et al., 2010). Corrections for U, Th, Pb

280 and REE matrix effects in monazite Pb/U and Pb/Th, and renormalization of

281 monazite $^{207}Pb/^{206}Pb$ data, were carried out subsequently applying

282 established protocols (Fletcher et al., 2010). Data plots were prepared using

283 Isoplot-3 (Ludwig, 2012). Individual analyses in concordia plots are displayed

284 with 1σ errors, whereas weighted mean dates are quoted with 95%

285 confidence limits, unless otherwise specified.

286

287 **RESULTS**

288 **Contrasting morphology and compositions of monazite**

289   Monazite in the gabbronorite sample WM5 occurs as euhedral or

290 subhedral crystals, up to 60 μm long, with aspect ratios between 2:1 and 3:1

291 (Fig. 4A, B). They show uniform Th abundances averaged at 35,000 ppm and

292 Th/U of 45, typical of igneous monazite (e.g., Zi et al., 2018). The monazite

293 exhibits pleochroic haloes in biotite (Fig. 3D). Acicular zircon crystals or

294 crystal aggregates also occur in this sample (Figs. 3D and 4C).

295   Monazite in muscovite schists from the Kabanga area displays two

296 distinct modes of crystal habit: discrete minute, hypidioblastic to xenoblastic

297 grains (<30 μm, Fig. 5A-C), and large, skeletal aggregates (>300 μm across;

298 Figs. 5D, 6A-C). Consistently, these two types of monazite show marked

299 differences in U and, in particular, Th concentrations (Fig. 7). The minute

300 monazite (e.g., sample K99 in Fig. 5A) is homogeneous in back-scattered

301 electron (BSE) images, with no or minimal inclusions. They have significantly

302 higher Th and U relative to the skeletal monazite (K89 and K96). The

303 compositional contrast is best illustrated by sample K100 in which both types

304 of monazite are observed (Fig. 5C, D), and the difference in Th between the

305 two types is greater than an order of magnitude (Fig. 7).

306

307 **Multiple generations of monazite growth**

308   U-Pb geochronology results are summarized in this section and in

309 Table 1; full datasets are provided in the Data Repository (Tables DR1-DR7).

310 The results are integrated with previously published geochronology data

311 (compiled in Table S2) for comparison purposes and to establish a complete

312 history for the emplacement of the igneous intrusions and associated

313 metamorphic-hydrothermal activities.

314

315 *Igneous monazite and zircon*

316   Monazite and zircon were identified in the gabbronorite sample (WM5)

317 (Figs. 3D, 4A-C). Twenty-seven analyses were collected from five monazite

318   grains, among which one analysis shows >1% common ^{206}Pb and >5%

319   discordance and was thus excluded in age calculation. The rest give a

320   weighted mean ^{207}Pb/^{206}Pb date of 1391 ± 9 Ma (*n* = 26, MSWD = 1.5) and

321   weighted mean ^{206}Pb/^{238}U date of 1395 ± 10 Ma (MSWD = 2.0) (Fig. 4D), with

322   the former being considered a better approximation of the timing of monazite

323   growth.

324   A total of 22 spot analyses were obtained on zircon from this sample;

325   five of them record >5% discordance and/or >1% common ^{206}Pb and hence

326   are disregarded in age determinations. The remaining 17 analyses, from nine

327   zircon grains, have a weighted mean ^{207}Pb/^{206}Pb date of 1387 ± 10 Ma

328   (MSWD = 0.85) and mean ^{206}Pb/^{238}U date of 1395 ± 18 Ma (MSWD = 0.83). It

329   is noted that most of the data show slight reverse discordance (Fig. 4E), likely

330   reflecting some extent of mass fractionation related to matrix effect. The mean

331   ^{207}Pb/^{206}Pb date of 1387 ± 10 Ma is taken as the zircon crystallization age.

332   Monazite and zircon in this sample show unequivocal characteristics of

333   igneous origin, and both are consistently uniform in Th and U chemistry,

334   indicating a single generation of each mineral. As the mean ^{207}Pb/^{206}Pb dates

335   of zircon and monazite are mutually indistinguishable within analytical

336   uncertainties, the datasets from the two independent chronometers can be

337   pooled to give a weighted mean ^{207}Pb/^{206}Pb date of 1389.5 ± 6.2 Ma (*n* = 43,

338   MSWD = 1.2), rounding to 1390 ± 7 Ma, which is considered as the best

339   estimate of the age of igneous crystallization.

340

341   ***Metamorphic monazite***

342   Monazite crystals in polished thin sections made from five metapelite

343   (muscovite schist and banded pelite) samples were analyzed. They occur as

344   authigenic grains surrounded by, and intergrown with, other metamorphic

345   minerals. As shown in Figures 5-8, the abundance, grain size, crystal

346   morphology and texture, chemical composition, and U-Th-Pb ages of the

347   authigenic monazite all vary as a function of metamorphic grade and host

348   lithology, and allow classification into three types corresponding to three

349   episodes of monazite growth, referred to as M-I, M-II, and M-III (Table 1).

350

351   *M-I monazite, K99 and K100*

352   M-I monazite occurs as discrete, minute (10–30 μm), hypidioblastic to

353   xenoblastic crystals in muscovite schist samples K99 and K100 (Fig. 5A, C)

354   collected from the upper portion of the Kabanga Main intrusion, and is

355   characterized by markedly high Th and U (typically >100,000 ppm and >2,000

356   ppm, respectively), with high Th/U values (most >50) (Fig. 7). Eight analyses

357   on 7 grains from the two samples display a significant variation in radiogenic

358   ^{238}U/^{206}Pb, but their radiogenic ^{207}Pb/^{206}Pb define a restricted range (Fig. 5E),

359   suggesting that all the grains are of the same age, but have lost variable

360   amounts of radiogenic Pb. Thorium-rich monazite has been shown to be more

361   susceptible to alteration than its Th-poor counterpart, likely due to greater

362   chemical disequilibrium at low temperatures or to radiation-induced partial

363   metamictization given the exceedingly high Th contents (Berger et al., 2008).

364   Excluding distinct outliers in ^{207}Pb/^{206}Pb, 8 analyses define an array

365   subparallel to the ^{238}U/^{206}Pb axis, only two of the ^{238}U/^{206}Pb apparent ages are

366   within 10% discordance, suggesting that almost all of the analyzed areas are

367 Pb deficient. The overall spread of the high-Th analyses in the concordia

368 diagram (Fig. 5E) suggests that Pb loss has resulted from a combination of

369 both geologically ancient and recent events. In that case, the best estimate of

370 the crystallisation age is given by the weighted mean ^{207}Pb/^{206}Pb date, 1402 ±

371 9 Ma (n = 8, MSWD = 0.33).

372   Monazite grain 0911K from sample K99 shows crystal morphology

373 (elongate, Fig. 5B) and Th-U chemistry (relatively low Th/U = 9, Fig. 7) distinct

374 from other grains, and one analysis on this grain yielded a ^{207}Pb/^{206}Pb date of

375 1378 ± 5 Ma (1σ), significantly younger than other grains from the same

376 sample but similar to the M-II monazite (see below). Monazite grain 0911A

377 from sample K100 displays an inclusion-bearing core enclosed by a brighter,

378 inclusion-free rim that shows a hypidioblastic crystal outline (Fig. 5C). The rim

379 is characterized by elevated Th and U (but lower Th/U ratio) compared with

380 the core, and possibly formed through dissolution-reprecipitation during a

381 younger metamorphic/hydrothermal event. Consistently, the spot analysis

382 (0911A.1-1) on the rim yielded a ^{207}Pb/^{206}Pb date of 1379 ± 8 Ma (1σ) which

383 is comparable with that recorded by grain 0911K.

384

385

386 *M-II monazite, K100, K89 and K96*

387   M-II monazite occurs as large (>300 µm), round or lozenge-shaped

388 poikiloblasts displaying skeletal textures (Figs. 5D, 6A-C), and mainly occurs

389 in samples K89 and K96, but is also seen in K100. These monazite grains are

390 characterized by lower Th and U contents (<10,000 ppm and <1,000 ppm,

391 respectively) with Th/U ratios typically <30 (Fig. 7). The marked similarities in

392 crystal texture and Th-U chemistry indicate that these grains likely formed
393 from the same metamorphic event.

394 Six analyses were taken from a skeletal grain in K100. Excluding 2
395 analyses which record >1% common ^{206}Pb or >10% reverse discordance and
396 one outlier, the rest yielded ^{207}Pb/^{206}Pb dates ranging from 1376 Ma to 1302
397 Ma; these together with the single analysis from the rim of monazite grain
398 0911A (Fig. 5C) in this sample, result in a weighted mean ^{207}Pb/^{206}Pb date of
399 1375 ± 15 Ma (n = 4, MSWD = 1.08) (Fig. 5E).

400 Twenty analyses were taken from three aggregate grains in sample
401 K89. Uranium and Th contents in these grains are low and variable, leading to
402 poor precision in age determination. Only 5 analyses have <1% common
403 ^{206}Pb and are within 5% of apparent discordance. They give a weighted mean
404 ^{207}Pb/^{206}Pb date of 1369 ± 34 Ma (MSWD = 1.09), but their ^{206}Pb/^{238}U ratios
405 are scattered (Fig. 6D). Applying less rigorous criteria, if the 4 analyses that
406 show slightly >1% common ^{206}Pb or marginally >5% discordance are taken
407 into account, the weighted mean ^{207}Pb/^{206}Pb age becomes 1379 ± 27 Ma (n =
408 9, MSWD = 1.1).

409 Twenty analyses performed on monazite in muscovite schist sample
410 K96 show overall uniformity of both U-Th compositions and U-Pb ages,
411 indicating a single generation. However, 6 analyses failed to satisfy the data
412 screen criteria with regard to common Pb and discordance levels, and thus
413 were disregarded in age determinations. The remaining 14 analyses yielded a
414 weighted mean ^{207}Pb/^{206}Pb date of 1374 ± 13 Ma (MSWD = 0.73) (Fig. 6E).

415   Pooled together, M-II monazite from the three samples yielded a

416 weighted mean ^{207}Pb/^{206}Pb date of 1375 ± 8 Ma (n = 25, MSWD = 1.17),

417 taken as the best estimate of the age of the monazite growth.

418

419 *M-III monazite, K101*

420   Fourteen analyses were taken from 5 monazite grains in the banded

421 pelite sample K101. Monazite occurs as inclusion-free, xenoblastic crystals in

422 association with biotite and is encased in plagioclase (Fig. 8A-B). The U and

423 Th contents are substantial (Fig. 7), leading to reasonably good precision in

424 ^{207}Pb/^{206}Pb despite young ages. All data show appreciable levels of common

425 ^{206}Pb, but none are >1%. Ten analyses are within 5% of discordance, and

426 give a weighted mean ^{207}Pb/^{206}Pb date of 991 ± 16 Ma (MSWD = 0.84)

427 (Fig. 7C). Consistently, the weighted mean of the corresponding ^{206}Pb/^{238}U

428 dates is 991 ± 11 Ma (n = 10, MSWD = 1.3), and the independently-calibrated

429 weighted mean ^{208}Pb/^{232}Th date for the same analyses is 988 ± 31 Ma. The

430 mean ^{207}Pb/^{206}Pb date of 991 ± 16 Ma is the preferred age of the M-III

431 monazite.

432

433 **DISCUSSION**

434 **Links between monazite growth and intrusion events**

435   Characterization based on crystal morphology and textural

436 relationships indicates that all the sedimentary rock-hosted monazite

437 investigated in this study is metamorphic in origin. The monazite is contained

438 in samples that comprise minerals clearly of metamorphic origin, including

439 recrystallized feldspar and sulfide minerals. Triple junctions and/or

440 interfingering textures observed between metamorphic monazite and
441 surrounding minerals (Figs. 5, 6, 8) indicate simultaneous growth.

442   The amount of Th in monazite from different rocks is widely variable,
443 and a correlation between Th abundance and metamorphic grade has long
444 been recognized (Overstreet, 1967), indicating that the variation of Th in
445 monazite is controlled by temperature-pressure conditions during
446 metamorphism. Numerous studies have shown that monazite precipitated in
447 low-grade metamorphic or hydrothermal environments typically has less than
448 1 wt.% ThO_2, whereas that from high-grade (amphibolite facies or higher)
449 rocks can contain up to 9 wt.% ThO_2 (Overstreet, 1967; Rasmussen et al.,
450 2001; Rasmussen and Fletcher, 2002; Schandl and Gorton, 2004; Zi et al.,
451 2015). The elevation of Th contents in high-grade monazite (Overstreet, 1967)
452 likely reflects the release of Th (and U) into metamorphic fluids by mineral
453 reactions (e.g., dissolution of detrital monazite), which also supplied the REEs
454 and phosphorous for the growth of authigenic monazite (Rasmussen and
455 Muhling, 2007; Rasmussen and Muhling, 2009).

456   The high- and low-Th monazite identified in the metasedimentary host
457 rocks of the igneous intrusions at Kabanga yielded two distinct U-Pb ages,
458 1402 ± 9 Ma and 1375 ± 8 Ma, respectively (Figs. 8 & 9). It is straightforward
459 that the minute, inclusion-free, monazite crystals (M-I) characterized by Th
460 enrichment were formed in high-grade contact metamorphic aureoles around
461 the mafic-ultramafic intrusions at ca. 1400 Ma, a date convergent with results
462 from the igneous monazite and zircon (Figs. 9 & 10). The monazite grains (M-
463 II) that display Th-depletion and skeletal textures most likely crystallized as a
464 consequence of low-grade metamorphism, as also supported by the

465 xenoblastic and inclusion-rich habit of these crystals. The low-grade

466 metamorphic activity at ca. 1375 Ma is more regional in nature and is

467 temporally and spatially related to emplacement of the S-type granites in the

468 KAB.

469 The M-III monazite, dated at 991 ± 16 Ma, from sample K101 shows

470 moderate Th and U compositions (Fig. 7) and its growth is readily linked to a

471 metamorphic/hydrothermal episode synchronous with the emplacement of the

472 tin-bearing granites and related regional-scale Sn mineralization in both the

473 KAB and KIB (Pohl, 1994; Kokonyangi et al., 2004; Kokonyangi et al., 2006;

474 Tack et al., 2010). Similar ages are also recorded by metamorphic zircon rims

475 (966 ± 11 Ma), from a S-type granite in the Kilimbi-Muzimu massif of the KAB

476 (Tack et al., 2010), suggesting regional-scale metamorphism, which gave rise

477 to the ca. 990 Ma monazite in the banded pelite at Kabanga.

478

479 **An updated igneous history: bimodal, but not coeval**

480 Earlier geochronology work carried out by Tack et al. (1994) yielded an

481 emplacement age of ca. 1275 Ma (U-Pb zircon age of an amphibole norite

482 from Musongati) for the KM mafic-ultramafic rocks, which has been

483 superseded by a new age of 1374 ± 14 Ma obtained from the same sample

484 (Tack et al., 2010). The widespread S-type granites that were imprecisely

485 dated at 1370-1110 Ma have also been narrowed down to 1380-1370 Ma (Fig.

486 10) (Deblond et al. 2001; Tack et al. 2010 and references therein). Although

487 the large variations in age constraints have caused conflicting interpretations

488 with regard to the mafic-ultramafic intrusions in relation to the S-type granites

489 and regional tectonics (e.g., Pohl, 1994; Tack et al., 1994), the new results of

490 Tack et al. (2010) led them to propose a short-lived, ca. 1375 Ma Kibaran

491 event that is marked by coeval, bimodal magmatism producing both the mafic-

492 ultramafic intrusions and the S-type granites in the KAB. The generation of the

493 voluminous S-type granites was attributed to concomitant, large-scale crustal

494 melting induced by emplacement of mantle-derived magma (Tack et al., 2010).

495   Our U-Pb geochronology results from monazite and zircon, however,

496 corroborate zircon ages of ca. 1400 Ma from mafic-ultramafic intrusions at

497 Kabanga North and Kapalagulu (Maier et al., 2007), and suggest that the

498 formation of the mafic-ultramafic intrusions took place approximately 25

499 million years before the emplacement of voluminous granites at ca. 1375 Ma

500 (Figs. 9 & 10). In support of this interpretation, the youngest detrital zircon

501 from the Muyinga Quartzite in the Western Domain yielded concordant

502 $^{207}Pb/^{206}Pb$ ages of 1421 ± 37 Ma and 1412 ± 21 Ma (1σ), and has been

503 interpreted to represent recycling of an underlying volcanic unit (Fernandez-

504 Alonso et al., 2012). It is likely that this ca. 1.4 Ga volcanism represents the

505 surface expression of KM mafic-ultramafic plutonism. A similar $^{207}Pb/^{206}Pb$

506 date (1417 ± 2 Ma) has been recorded by zircon from a mafic

507 (orthoamphibolite) complex at Mitwaba in the KIB (Kokonyangi et al., 2005).

508   The large spread (1393 ± 12 Ma to 1148 ± 50 Ma) shown by the most

509 concordant zircon analyses from an amphibole-norite sample (Mutanga)

510 (Tack et al., 2010) suggest Pb-loss and/or partial resetting of the U-Pb

511 systems during later thermal events, therefore, even the weighted mean age

512 of 1374 ± 14 Ma derived from the oldest cluster likely represents a minimum

513 crystallization age of the rock. This is in agreement with $^{40}Ar/^{39}Ar$ data of

514 1379-1340 Ma obtained from the mafic-ultramafic intrusions, interpreted as

cooling ages of the igneous bodies (Deblond et al., 2001; Tack et al., 2010). The about 25 million-year difference between the weighted mean ages of the mafic-ultramafic intrusions and the S-type granites indicates a significant age gap (Figs. 9 & 10), which is at odds with the proposed "coeval" and "bimodal" nature of the magmatism (Tack et al., 2010). The postulated cogenetic emplacement and geodynamic setting of the mafic and felsic rocks thus also requires re-evaluation.

Tectonic imprints: from Nuna breakup to Rodinia assembly

The ability to determine the intrusive ages of mafic-ultramafic rocks is critically important for supercontinent reconstructions and for the global correlation of ancient mafic magmatic activity worldwide (Ernst et al., 2008; Ernst et al., 2013). On a global scale, the 1.40-1.37 Ga magmatic rocks in the KAB may be compared directly with the contemporaneous components in the different blocks including the Congo Craton (Mayer et al., 2004), Western African Craton (El Bahat et al., 2013), Kalahari (Hanson et al., 2006), Yilgarn (Stark et al., 2018), Siberia, Baltica, and Laurentia (Ernst and Buchan, 2001; Upton et al., 2005; Verbaas et al., 2018), and are correlated to represent mafic magmatic outbursts during the breakup of the Nuna supercontinent (Ernst et al., 2008; Evans and Mitchell, 2011; Pisarevsky et al., 2014).

Mafic-ultramafic layered intrusions at Kabanga, Musongati and Kapalagulu show broad similarities in crystallization sequences and mineral compositions (Maier et al., 2008) and hence have been regarded as an integrated igneous belt approximately 500 km long (Maier et al., 2010). Mafic intrusions typically act as markers of pre-existing crustal weakness and their

occurrences as indicators of intraplate crustal extension associated with processes such as subduction (back-arc extension), mantle plume impingement and continental rifting during supercontinent breakup (e.g., Wilson, 1992; Ernst et al., 2013). Geochemical characteristics of the KM intrusions indicate a parental magma predominantly derived from the asthenospheric mantle with appreciable assimilation of pelitic sedimentary rocks during magma ascent and emplacement, leading to sulfide enrichment of the intrusions (Maier et al., 2010). Mäkitie et al. (2014) correlate these mafic-ultramafic intrusions to the arcuate mafic dikes (the Lake Victoria dike swarm) in the periphery of the KAB (Fig. 1) and suggest that they collectively form a large igneous province, despite the considerable differences in geochemistry of the two suites. However, synchroneity between the dike swarm and the ca. 1.4 Ga mafic-ultramafic intrusions remains to be confirmed, considering the large uncertainties of the available Sm-Nd isochron age constraints for the dike swarm (1368 ± 41 Ma and 1374 ± 42 Ma; Mäkitie et al., 2014).

The 'Wilson-style orogenic' or 'active margin' model previously proposed for the Mesoproterozoic evolution of the KAB was refuted by Fernandez-Alonso et al. (2012) who, largely based on regional correlation of basin stratigraphy and depositional history, argue for an intracratonic setting for the KAB since the Paleoproterozoic (ca. 1.8 Ga) formation of a united 'proto-Congo Craton'. Instead, the linear distribution of the mafic-ultramafic intrusions along the western margin of the Tanzania Craton is consistent with a lithospheric-scale structural control, in an extensional regime, to allow emplacement of the mantle-derived melts into the KAB pelitic sedimentary

rocks. Stratigraphic successions and provenance analysis of the KAB suggest that the attempted rifting was aborted (Fernandez-Alonso et al., 2012), and that the mafic-ultramafic intrusions and the subsequent intracrustal melting, exemplified by the S-type granitic plutonism during peak Kibaran event at ca. 1375 Ma (Tack et al., 2010), likely marked the final consolidation of this part of the assembled proto-Congo Craton (Fernandez-Alonso et al., 2012).

Renewed crustal melting took place at ca. 990 Ma, possibly after an episode of A-type granite plutonism at ca. 1205 Ma (Tack et al., 2010), and gave rise to regional-scale tin-bearing granites and numerous pegmatitic and quartz veins rich in Sn, W, and rare metals (Cahen et al., 1984; Pohl, 1994). The tin-bearing granites and associated mineralization are related to a compressive deformation (the S2-fabric as documented by Fernandez-Alonso et al. (2012); see also Pohl (1994)) which is considered a far-field effect from the Irumide Belt during amalgamation of the Rodinia supercontinent (De Waele et al., 2003; Johnson et al., 2005), although whether or not the proto-Congo Craton (including the KAB) was a component of Rodinia, remains an open question (De Waele et al., 2008; Pisarevsky et al., 2014).

Implications for dating mafic-ultramafic intrusions by monazite

The interaction between hot intrusions and surrounding sediments leads to contact metamorphism (Einsele et al., 1980) that results in the growth of authigenic monazite (Williams, 2001; Rasmussen and Fletcher, 2002). Our study demonstrates that metamorphic monazite in hornfels (contact aureoles) can be dated *in situ* by ion microprobe using a small ablation spot. By characterizing textural relationships, crystal morphology and chemistry,

590   multiple generations of monazite can be distinguished and linked to regional-

591   scale tectonic and magmatic activities that provided the heat and fluids for

592   their growth. Therefore, U-Pb dating of metamorphic monazite in hornfels are

593   capable of not only constraining individual intrusion events, but also providing

594   a more complete picture of the metamorphic history of the host terrane.

595   Ni (-PGE) mineralization is genetically related to igneous processes of

596   mafic-ultramafic intrusions (Naldrett, 1999, 2010). The mafic-ultramafic bodies

597   hosting the nickel sulfide and PGE deposits are typically small and irregular in

598   dimension, and precise geochronology is essential to understanding the

599   emplacement history and geodynamic setting of the intrusions, which help to

600   locate mineralized intrusive bodies (Maier and Groves, 2011). The results of

601   this study demonstrate the potential of using monazite from hornfels adjoining

602   mineralized mafic-ultramafic rocks to precisely constrain the timing and

603   duration of mafic-ultramafic magmatism in the East African Nickel Belt and

604   assess the relationships between mafic-ultramafic and granitic magmatism.

605   The approach employed in the present study, therefore, provides an

606   additional avenue for resolving the commonly complicated magmatic and

607   metamorphic history of economically important intrusions as well as the

608   regional tectonothermal history of the host terranes.

609

610

611   **CONCLUSIONS**

612   Precise and accurate dating of mafic-ultramafic intrusive rocks has

613   been one of the most challenging and controversial aspects in attempting to

614   understand their geology and nickel sulfide mineralization. Using the KM

alignment of the East African Nickel Belt as an example, we report the U-Pb geochronology of metamorphic monazite in contact aureoles of mineralized mafic-ultramafic intrusions. *In situ* U-Pb geochronology of monazite crystals reveals three episodes of metamorphism in the KAB, including: i) Contact metamorphism (ca. 1400 Ma) related to the mafic-ultramafic intrusions; ii) a regional metamorphic event (ca. 1375 Ma) linked to intracrustal melting and intrusion of S-type granites; iii) a regional metamorphic event (ca. 990 Ma) that was accompanied by intracrustal melting to produce the tin-bearing granites.

In particular, the documentation of metamorphic monazite in hornfels of the mafic-ultramafic intrusions is significant as a means of establishing indirect emplacement ages, to circumvent difficulties of directly dating such rocks. The similarity of the metamorphic monazite ages and those from igneous monazite and zircon in a differentiated phase of the intrusions adds confidence to the reliability of the technique. Despite the overlap in ranges between some of the age determinations, the mean ages acquired in this study, i.e., the ca. 1400 Ma for contact metamorphism associated with the mafic-ultramafic rocks and ca. 1375 Ma syn-Kibaran metamorphism, are consistent with the crosscutting relationships between the KM mafic-ultramafic intrusions and the S-type granites, indicating a substantial age difference of approximately 25 million years. As such, monazite in metamorphosed sedimentary rocks not only provide age records that perfectly match known igneous history, but also resolve that the mafic-ultramafic layered intrusions significantly predated the pervasive granitic magmatism, thus invalidating the

639 coeval bimodal model (the ca. 1375 Ma Kibaran event) as previously

640 proposed.

641   The ca. 1400 Ma mafic-ultramafic intrusions and the following granitic

642 plutonism during the ca. 1375 Ma Kibaran event in the KAB and adjoining

643 areas represent a significant component of the global-scale igneous event

644 which is linked to the breakup of the Nuna supercontinent. The renewed

645 crustal melting that gave rise to the ca. 990 Ma tin-bearing granites is readily

646 ascribed to tectonic imprint related to collision processes along the Irumide

647 Belt during Rodinia assembly.

648

658

659 **REFERENCES CITED**

660 Arndt, N. T., Czamanske, G. K., Walker, R. J., Chauvel, C., and Fedorenko, V. A.,
661   2003, Geochemistry and Origin of the Intrusive Hosts of the Noril'sk-Talnakh
662   Cu-Ni-PGE Sulfide Deposits: Economic Geology, v. 98, no. 3, p. 495-515.
663 Ayers, J. C., Crombie, S., Loflin, M., Miller, C. F., and Luo, Y., 2013, Country rock
664   monazite response to intrusion of the Searchlight pluton, southern Nevada:
665   American Journal of Science, v. 313, no. 4, p. 345-394.

666 Begg, G. C., Hronsky, J. A. M., Arndt, N. T., Griffin, W. L., O'Reilly, S. Y., and
667   Hayward, N., 2010, Lithospheric, Cratonic, and Geodynamic Setting of Ni-
668   Cu-PGE Sulfide Deposits: Economic Geology, v. 105, no. 6, p. 1057−1070.
669 Berger, A., Gnos, E., Janots, E., Fernandez, A., and Giese, J., 2008, Formation and
670   composition of rhabdophane, bastnäsite and hydrated thorium minerals during
671   alteration: Implications for geochronology and low-temperature processes:
672   Chemical Geology, v. 254, no. 3, p. 238-248.
673 Black, L. P., Kinny, P. D., and Sheraton, J. W., 1991, The difficulties of dating mafic
674   dykes: an Antarctic example: Contributions to Mineralogy and Petrology, v.
675   109, no. 2, p. 183-194.
676 Buchwaldt, R., Toulkeridis, T., Todt, W., and Ucakuwun, E. K., 2008, Crustal age
677   domains in the Kibaran belt of SW-Uganda: Combined zircon geochronology
678   and Sm–Nd isotopic investigation: Journal of African Earth Sciences, v. 51, no.
679   1, p. 4-20.
680 Cahen, L., Snelling, N. J., Delhal, J., Vail, J. R., Bonhomme, M., and Ledent, D.,
681   1984, The geochronology and evolution of Africa, Oxford, Oxford University
682   Press, 512 p.:
683 Chamberlain, K. R., Schmitt, A. K., Swapp, S. M., Harrison, T. M., Swoboda-Colberg,
684   N., Bleeker, W., Peterson, T. D., Jefferson, C. W., and Khudoley, A. K., 2010,
685   In situ U–Pb SIMS (IN-SIMS) micro-baddeleyite dating of mafic rocks:
686   Method with examples: Precambrian Research, v. 183, no. 3, p. 379-387.
687 De Waele, B., Johnson, S. P., and Pisarevsky, S. A., 2008, Palaeoproterozoic to
688   Neoproterozoic growth and evolution of the eastern Congo Craton: Its role in
689   the Rodinia puzzle: Precambrian Research, v. 160, no. 1, p. 127-141.
690 Deblond, A., Punzalan, L. E., Boven, A., and Tack, L., 2001, The Malagarazi
691   supergroup of southeast Burundi and its correlative Bukoba supergroup of
692   northwest Tanzania: neo- and mesoproterozoic chronostratigraphic constraints
693   from Ar-Ar ages on mafic intrusive rocks: Journal of African Earth Sciences,
694   v. 32, no. 3, p. 435-449.
695 Deblond, A., and Tack, L., 1999, Main characteristics and review of mineral
696   resources of the Kabanga-Musongati mafic-ultramafic alignment in Burundi:
697   Journal of African Earth Sciences, v. 29, no. 2, p. 313-328.
698 Duchesne, J.-C., Liégeois, J.-P., Deblond, A., and Tack, L., 2004, Petrogenesis of the
699   Kabanga–Musongati layered mafic–ultramafic intrusions in Burundi (Kibaran
700   Belt): geochemical, Sr–Nd isotopic constraints and Cr–Ni behaviour: Journal
701   of African Earth Sciences, v. 39, no. 3–5, p. 133-145.
702 Einsele, G., Gieskes, J. M., Curray, J., Moore, D. M., Aguayo, E., Aubry, M.-P.,
703   Fornari, D., Guerrero, J., Kastner, M., Kelts, K., Lyle, M., Matoba, Y.,
704   Molina-Cruz, A., Niemitz, J., Rueda, J., Saunders, A., Schrader, H., Simoneit,
705   B., and Vacquier, V., 1980, Intrusion of basaltic sills into highly porous
706   sediments, and resulting hydrothermal activity: Nature, v. 283, no. 5746, p.
707   441-445.
708 El Bahat, A., Ikenne, M., Söderlund, U., Cousens, B., Youbi, N., Ernst, R.,
709   Soulaimani, A., El Janati, M. h., and Hafid, A., 2013, U–Pb baddeleyite ages
710   and geochemistry of dolerite dykes in the Bas Drâa Inlier of the Anti-Atlas of
711   Morocco: Newly identified 1380Ma event in the West African Craton: Lithos,
712   v. 174, p. 85-98.
713 Ernst, R. E., Bleeker, W., Söderlund, U., and Kerr, A. C., 2013, Large Igneous
714   Provinces and supercontinents: Toward completing the plate tectonic
715   revolution: Lithos, v. 174, no. Supplement C, p. 1-14.

716 Ernst, R. E., and Buchan, K. L., 2001, Large mafic magmatic events through time and
717   links to mantle-plume heads, *in* Ernst, R. E., and Buchan, K. L., eds., Mantle
718   Plumes: Their Identification Through Time, Volume 352: Boulder, Colorado,
719   p. 483-575.
720 Ernst, R. E., Wingate, M. T. D., Buchan, K. L., and Li, Z. X., 2008, Global record of
721   1600–700 Ma Large Igneous Provinces (LIPs): Implications for the
722   reconstruction of the proposed Nuna (Columbia) and Rodinia supercontinents:
723   Precambrian Research, v. 160, no. 1–2, p. 159-178.
724 Evans, D. A. D., 2013, Reconstructing pre-Pangean supercontinents: Geological
725   Society of America Bulletin, v. 125, no. 11-12, p. 1735-1751.
726 Evans, D. A. D., and Mitchell, R. N., 2011, Assembly and breakup of the core of
727   Paleoproterozoic–Mesoproterozoic supercontinent Nuna: Geology, v. 39, no. 5,
728   p. 443-446.
729 Evans, D. M., Boadi, I., Byemelwa, L., Gilligan, J., kabete, J., and Marcet, P., 2000,
730   Kabanga magmatic nickel sulphide deposits, Tanzania: morphology and
731   geochemistry of associated intrusions: Journal of African Earth Sciences, v. 30,
732   no. 3, p. 651-674.
733 Evans, D. M., Byemelwa, L., and Gilligan, J., 1999, Variability of magmatic sulphide
734   compositions at the Kabanga nickel prospect, Tanzania: Journal of African
735   Earth Sciences, v. 29, no. 2, p. 329-351.
736 Evans, D. M., Hunt, J. P. P. M., and Simmonds, J. R., 2016, An Overview of Nickel
737   Mineralisation in Africa with Emphasis on the Mesoproterozoic East African
738   Nickel Belt (EANB): Episodes, v. 39, no. 2, p. 319.
739 Fernandez-Alonso, M., Cutten, H., De Waele, B., Tack, L., Tahon, A., Baudet, D.,
740   and Barritt, S. D., 2012, The Mesoproterozoic Karagwe-Ankole Belt (formerly
741   the NE Kibara Belt): The result of prolonged extensional intracratonic basin
742   development punctuated by two short-lived far-field compressional events:
743   Precambrian Research, v. 216, p. 63-86.
744 Fletcher, I. R., McNaughton, N. J., Davis, W. J., and Rasmussen, B., 2010, Matrix
745   effects and calibration limitations in ion probe U–Pb and Th–Pb dating of
746   monazite: Chemical Geology, v. 270, no. 1–4, p. 31-44.
747 Hanson, R. E., Harmer, R. E., Blenkinsop, T. G., Bullen, D. S., Dalziel, I. W. D.,
748   Gose, W. A., Hall, R. P., Kampunzu, A. B., Key, R. M., Mukwakwami, J.,
749   Munyanyiwa, H., Pancake, J. A., Seidel, E. K., and Ward, S. E., 2006,
750   Mesoproterozoic intraplate magmatism in the Kalahari Craton: A review:
751   Journal of African Earth Sciences, v. 46, no. 1, p. 141-167.
752 Harlov, D., Wirth, R., and Hetherington, C., 2011, Fluid-mediated partial alteration in
753   monazite: the role of coupled dissolution–reprecipitation in element
754   redistribution and mass transfer: Contributions to Mineralogy and Petrology, v.
755   162, no. 2, p. 329-348.
756 Heaman, L. M., 2009, The application of U–Pb geochronology to mafic, ultramafic
757   and alkaline rocks: An evaluation of three mineral standards: Chemical
758   Geology, v. 261, no. 1–2, p. 43-52.
759 Heaman, L. M., and LeCheminant, A. N., 1993, Paragenesis and U-Pb systematics of
760   baddeleyite (ZrO2): Chemical Geology, v. 110, no. 1–3, p. 95-126.
761 Hulbert, L. J., Hamilton, M. A., Horan, M. F., and Scoates, R. F. J., 2005, U-Pb
762   Zircon and Re-Os Isotope Geochronology of Mineralized Ultramafic
763   Intrusions and Associated Nickel Ores from the Thompson Nickel Belt,
764   Manitoba, Canada: Economic Geology, v. 100, no. 1, p. 29.

Kokonyangi, J., Armstrong, R., Kampunzu, A. B., Yoshida, M., and Okudaira, T.,
    2004, U–Pb zircon geochronology and petrology of granitoids from Mitwaba
    (Katanga, Congo): implications for the evolution of the Mesoproterozoic
    Kibaran belt: Precambrian Research, v. 132, no. 1, p. 79-106.

Kokonyangi, J., Kampunzu, A. B., Poujol, M., Okudaira, T., Yoshida, M., and
    Shabeer, K. P., 2005, Petrology and geochronology of Mesoproterozoic
    mafic–intermediate plutonic rocks from Mitwaba (D. R. Congo): implications
    for the evolution of the Kibaran belt in central Africa: Geological Magazine, v.
    142, no. 1, p. 109.

Kokonyangi, J. W., Kampunzu, A. B., Armstrong, R., Yoshida, M., Okudaira, T.,
    Arima, M., and Ngulube, D. A., 2006, The Mesoproterozoic Kibaride belt
    (Katanga, SE D.R. Congo): Journal of African Earth Sciences, v. 46, no. 1, p.
    1-35.

Ludwig, K. R., 2009, Squid 2.50, A User's Manual, Berkeley, Berkeley
    Geochronology Centre, Berkeley Geochronology Centre Special Publication,
    104 p.:

-, 2012, User's Manual for Isoplot 3.75: A geochronological toolkit for Microsoft
    Excel, Berkeley, Berkeley Geochronology Centre, Berkeley Geochronology
    Centre Special Publication 75 p.:

Mäkitie, H., Data, G., Isabirye, E., Mänttäri, I., Huhma, H., Klausen, M. B., Pakkanen,
    L., and Virransalo, P., 2014, Petrology, geochronology and emplacement
    model of the giant 1.37Ga arcuate Lake Victoria Dyke Swarm on the margin
    of a large igneous province in eastern Africa: Journal of African Earth
    Sciences, v. 97, p. 273-296.

Maier, W. D., Barnes, S.-J., Sarkar, A., Ripley, E., Li, C., and Livesey, T., 2010, The
    Kabanga Ni sulfide deposit, Tanzania: I. Geology, petrography, silicate rock
    geochemistry, and sulfur and oxygen isotopes: Mineralium Deposita, v. 45, no.
    5, p. 419-441.

Maier, W. D., Barnes, S. J., Bandyayera, D., Livesey, T., Li, C., and Ripley, E., 2008,
    Early Kibaran rift-related mafic–ultramafic magmatism in western Tanzania
    and Burundi: Petrogenesis and ore potential of the Kapalagulu and Musongati
    layered intrusions: Lithos, v. 101, no. 1, p. 24-53.

Maier, W. D., and Groves, D. I., 2011, Temporal and spatial controls on the formation
    of magmatic PGE and Ni–Cu deposits: Mineralium Deposita, v. 46, no. 8, p.
    841-857.

Maier, W. D., Peltonen, P., and Livesey, T., 2007, The ages of the Kabanga north and
    Kapalagulu intrusions, Western Tanzania: a reconnaissance study: Economic
    Geology, v. 102, no. 1, p. 147.

Maier, W. D., Rasmussen, B., Fletcher, I. R., Godel, B., Barnes, S. J., Fisher, L. A.,
    Yang, S. H., Huhma, H., and Lahaye, Y., 2015, Petrogenesis of the ~2·77 Ga
    Monts de Cristal Complex, Gabon: Evidence for Direct Precipitation of Pt-
    arsenides from Basaltic Magma: Journal of Petrology, v. 56, no. 7, p. 1285-
    1308.

Mayer, A., Hofmann, A. W., Sinigoi, S., and Morais, E., 2004, Mesoproterozoic Sm-
    Nd and U-Pb ages for the Kunene Anorthosite Complex of SW Angola:
    Precambrian Research, v. 133, no. 3-4, p. 187-206.

Naldrett, A. J., 1999, World-class Ni-Cu-PGE deposits: key factors in their genesis:
    Mineralium Deposita, v. 34, no. 3, p. 227-240.

-, 2010, Secular Variation of Magmatic Sulfide Deposits and Their Source Magmas:
    Economic Geology, v. 105, no. 3, p. 669.

815   Overstreet, W. C., 1967, The geologic occurrence of monazite, 530.
816   Parrish, R. R., 1990, U–Pb dating of monazite and its application to geological
817   problems: Canadian Journal of Earth Sciences, v. 27, no. 11, p. 1431-1450.
818   Pisarevsky, S. A., Elming, S.-Å., Pesonen, L. J., and Li, Z.-X., 2014, Mesoproterozoic
819   paleogeography: Supercontinent and beyond: Precambrian Research, v. 244, p.
820   207-225.
821   Pohl, W., 1994, Metallogeny of the northeastern Kibara belt, Central Africa—Recent
822   perspectives: Ore Geology Reviews, v. 9, no. 2, p. 105-130.
823   Rasmussen, B., and Fletcher, I. R., 2002, Indirect dating of mafic intrusions by
824   SHRIMP U–Pb analysis of monazite in contact metamorphosed shale: an
825   example from the Palaeoproterozoic Capricorn Orogen, Western Australia:
826   Earth and Planetary Science Letters, v. 197, no. 3–4, p. 287-299.
827   -, 2004, Zirconolite: A new U-Pb chronometer for mafic igneous rocks: Geology, v.
828   32, no. 9, p. 785-788.
829   -, 2010, Dating sedimentary rocks using in situ U-Pb geochronology of syneruptive
830   zircon in ash-fall tuffs <1 mm thick: Geology, v. 38, no. 4, p. 299-302.
831   Rasmussen, B., Fletcher, I. R., and McNaughton, N. J., 2001, Dating low-grade
832   metamorphic events by SHRIMP U-Pb analysis of monazite in shales:
833   Geology, v. 29, no. 10, p. 963-966.
834   Rasmussen, B., Mueller, A., and Fletcher, I., 2009, Zirconolite and xenotime U–Pb
835   age constraints on the emplacement of the Golden Mile Dolerite sill and gold
836   mineralization at the Mt Charlotte mine, Eastern Goldfields Province, Yilgarn
837   Craton, Western Australia: Contributions to Mineralogy and Petrology, v. 157,
838   no. 5, p. 559-572.
839   Rasmussen, B., and Muhling, J., 2007, Monazite begets monazite: evidence for
840   dissolution of detrital monazite and reprecipitation of syntectonic monazite
841   during low-grade regional metamorphism: Contributions to Mineralogy and
842   Petrology, v. 154, no. 6, p. 675-689.
843   Rasmussen, B., and Muhling, J. R., 2009, Reactions destroying detrital monazite in
844   greenschist-facies sandstones from the Witwatersrand basin, South Africa:
845   Chemical Geology, v. 264, no. 1–4, p. 311-327.
846   Schandl, E. S., and Gorton, M. P., 2004, A textural and geochemical guide to the
847   identification of hydrothermal monazite: Criteria for selection of samples for
848   dating epigenetic hydrothermal ore deposits: Economic Geology, v. 99, no. 5,
849   p. 1027.
850   Scherstén, A., Årebäck, H., Cornell, D., Hoskin, P., Åberg, A., and Armstrong, R.,
851   2000, Dating mafic–ultramafic intrusions by ion-microprobing contact-melt
852   zircon: examples from SW Sweden: Contributions to Mineralogy and
853   Petrology, v. 139, no. 1, p. 115-125.
854   Scoates, J. S., Scoates, R. F. J., Wall, C. J., Friedman, R. M., and Couëslan, C. G.,
855   2017, Direct dating of ultramafic sills and mafic intrusions associated with Ni-
856   sulfide mineralization in the Thompson Nickel Belt, Manitoba, Canada:
857   Economic Geology, v. 112, no. 3, p. 675.
858   Seydoux-Guillaume, A.-M., Montel, J.-M., Bingen, B., Bosse, V., de Parseval, P.,
859   Paquette, J.-L., Janots, E., and Wirth, R., 2012, Low-temperature alteration of
860   monazite: Fluid mediated coupled dissolution–precipitation, irradiation
861   damage, and disturbance of the U–Pb and Th–Pb chronometers: Chemical
862   Geology, v. 330–331, p. 140-158.
863   Stark, J. C., Wang, X.-C., Li, Z.-X., Denyszyn, S. W., Rasmussen, B., and Zi, J.-W.,
864   2018, 1.39 Ga mafic dyke swarm in southwestern Yilgarn Craton marks Nuna

865   to Rodinia transition in the West Australian Craton: Precambrian Research, v.
866   316, p. 291-304.

867 Tack, L., Wingate, M. T. D., De Waele, B., Meert, J., Belousova, E., Griffin, B.,
868   Tahon, A., and Fernandez-Alonso, M., 2010, The 1375Ma "Kibaran event" in
869   Central Africa: Prominent emplacement of bimodal magmatism under
870   extensional regime: Precambrian Research, v. 180, no. 1, p. 63-84.

871 Upton, B. G. J., Rämö, O. T., Heaman, L. M., Blichert-Toft, J., Kalsbeek, F., Barry, T.
872   L., and Jepsen, H. F., 2005, The Mesoproterozoic Zig-Zag Dal basalts and
873   associated intrusions of eastern North Greenland: mantle plume–lithosphere
874   interaction: Contributions to Mineralogy and Petrology, v. 149, no. 1, p. 40-56.

875 Verbaas, J., Thorkelson, D. J., Milidragovic, D., Crowley, J. L., Foster, D., Daniel
876   Gibson, H., and Marshall, D. D., 2018, Rifting of western Laurentia at 1.38 Ga:
877   The Hart River sills of Yukon, Canada: Lithos, v. 316-317, p. 243-260.

878 Wilhelmij, H. R., and Cabri, L. J., 2016, Platinum mineralization in the Kapalagulu
879   Intrusion, western Tanzania: Mineralium Deposita, v. 51, no. 3, p. 343-367.

880 Williams, I. S., 2001, Response of detrital zircon and monazite, and their U–Pb
881   isotopic systems, to regional metamorphism and host-rock partial melting,
882   Cooma Complex, southeastern Australia*: Australian Journal of Earth
883   Sciences, v. 48, no. 4, p. 557-580.

884 Williams, M. L., Jercinovic, M. J., Harlov, D. E., Budzyń, B., and Hetherington, C. J.,
885   2011, Resetting monazite ages during fluid-related alteration: Chemical
886   Geology, v. 283, no. 3–4, p. 218-225.

887 Williams, M. L., Jercinovic, M. J., and Hetherington, C. J., 2007, Microprobe
888   Monazite Geochronology: Understanding Geologic Processes by Integrating
889   Composition and Chronology: Annual Review of Earth and Planetary
890   Sciences, v. 35, no. 1, p. 137-175.

891 Wilson, M., 1992, Magmatism and continental rifting during the opening of the South
892   Atlantic Ocean: a consequence of Lower Cretaceous super-plume activity?:
893   Geological Society, London, Special Publications, v. 68, no. 1, p. 241-255.

894 Zi, J.-W., Gregory, C. J., Rasmussen, B., Sheppard, S., and Muhling, J. R., 2017,
895   Using monazite geochronology to test the plume model for carbonatites: The
896   example of Gifford Creek Carbonatite Complex, Australia: Chemical Geology,
897   v. 463, p. 50-60.

898 Zi, J.-W., Rasmussen, B., Muhling, J. R., and Fletcher, I. R., 2018, U-Pb
899   geochronology of monazite in Precambrian tuffs reveals depositional and
900   metamorphic histories: Precambrian Research, v. 313, p. 109-118.

901 Zi, J.-W., Rasmussen, B., Muhling, J. R., Fletcher, I. R., Thorne, A. M., Johnson, S.
902   P., Cutten, H. N., Dunkley, D. J., and Korhonen, F. J., 2015, In situ U–Pb
903   geochronology of xenotime and monazite from the Abra polymetallic deposit
904   in the Capricorn Orogen, Australia: Dating hydrothermal mineralization and
905   fluid flow in a long-lived crustal structure: Precambrian Research, v. 260, no.
906   0, p. 91-112.

907

908   **Figure Captions**

909   **Figure 1**

910   Geological map showing distribution of the Karagwe-Ankole Belt (KAB)

911   metasedimentary rocks, granitoids and mafic-ultramafic intrusions in the

912   Kabanga-Musonggati alignment and adjoining areas. The inset map shows

913   location and extent of the recently redefined KAB and the Kibaran Belt (KIB)

914   (modified after Tack et al. 2010, Fernandez-Alonso et al. 2012, Evans et al.

915   2016 and references therein)

916   **Figure 2**

917   (A) Schematic geological map and cross section of the Kabanga area

918   showing main lithologies and their distribution. (B) Local map showing outcrop

919   and surface projections of mafic-ultramafic intrusions and massive sulfide ore

920   bodies. Locations of selected drill-holes are also shown. (C) Cross section

921   showing outlines of Kabanga Main and MNB (Main North Body) intrusions and

922   main ore zones. Maps and cross sections after Maier et al. (2010).

923   **Figure 3**

924   Drill-cores of Kabanga sedimentary rocks showing (A) Bleached contact zone

925   in hornfels (best illustrated by the drill-cores on the right) adjacent to

926   ultramafic rock, Kabanga Main, KN05-01, 138 m; (B) Sulfidic andalusite–

927   muscovite schist, MNB, KN01-05, 538 m; and (C) Banded pelite, MNB, KN01-

928   01, 1,645 m (from Maier et al. 2010). Photomicrographs of (D) gabbronorite

929   containing igneous zircon and monazite, monazite is surrounded by a

930   prominent pleochroic halo in biotite, sample WM5 from Kabanga Main, KN95-

931   78, 211.1 m, (E) muscovite schist, sample K96 from MNB, KN01-01B,

932   1356.15 m; (F) skeletal monazite hosted in muscovite schist, sample K100

933   from Kabanga Upper, KSM06, 125.4 m; (G, H) muscovite schist hosting

934   minute metamorphic monazite crystals under plane- and cross-polarized light,

935   respectively, sample K100 from Kabanga Upper, KSM06, 125.4 m, and (I)

936   banded pelite, sample K101 Kabanga Upper, KSM04, 150.4 m.

937   **Figure 4**

938   (A-C) Back-scattered electron (BSE) images of igneous monazite and zircon.

939   Dashed ellipses mark the area of each grain analysed by SHRIMP. (D)

940   Concordia plot and weighted mean ages of igneous monazite. (E) Concordia

941   plot and weighted mean ages of igneous zircon. 1σ analytical uncertainties

942   are displayed.

943   **Figure 5**

944   (A-D) BSE images of metamorphic monazite in muscovite schists (K99 and

945   K100) from Kabanga. Dashed ellipses mark the area of each grain analysed

946   by SHRIMP, in D the small analytical areas are indicated by black arrows. (E)

947   Concordia plot and weighted mean ages of metamorphic monazite. 1σ

948   analytical uncertainties are displayed.

949   **Figure 6**

950   (A-C) BSE images of metamorphic monazite in muscovite schists (K89) from

951   Nyanzali. Dashed ellipses mark the area of each grain analyzed by SHRIMP,

952   and are indicated by black arrows. (D, E) Concordia plots and weighted mean

953   ages of metamorphic monazite. 1σ analytical uncertainties are displayed.

954   **Figure 7**

955   Th-U plot displaying contrasting Th and U concentrations between igneous

956   and metamorphic monazites, and between the metamorphic monazites of

957   different age groups.

Figure 8

(A-B) BSE images of metamorphic monazite in banded pelite (K101) from Kabanga. Dashed ellipses mark the area of each grain analysed by SHRIMP. (C) Concordia plot and weighted mean ages of metamorphic monazite. 1σ analytical uncertainties are displayed.

Figure 9

(A) Probability density plots and histograms of all analyses from metamorphic monazites showing the bimodal distribution of the older cluster which is resolvable into two ages (1402 ± 9 Ma and 1375 ± 8 Ma), plus a distinct younger cluster at 991 ± 16 Ma. (B) Dates from the igneous zircon and monazite are overlapping which together yielded a pooled, weighted mean $^{207}Pb/^{206}Pb$ age of 1390 ± 8 Ma. Pooled ages are quoted at 95% confidence level. 20 Ma bin width.

Figure 10

Summary diagram of geochronology results obtained in this study in comparison with published data (compiled in Table S2). Data source: 1-9, this study; 10-11, Maier et al. (2007); 12-20 and 27-28, Tack et al. (2010); 21-24, Deblond et al. (2001); 25-26, Mäkitie et al. (2014).

TABLE 1. SUMMARY OF GEOCHRONOLOGY SAMPLES AND RESULTS

| Sample ID	Lithology	Dated mineral	Crystal morphology	Crystal size (μm)	Th content (wt.%)	Age* (Ma)	Av. Age[†] (Ma)
Igneous							
WM5	Gabbronorite	Monazite	Euhedral	50-70	~3	1391 ± 9	1390 ± 7
WM5	Gabbronorite	Zircon	Acicular, euhedral	Small	<0.05	1387 ± 10	
Metamorphic M I							
K99,	Muscovite schist	Monazite	Hypidioblast	15-30	9-20	1401± 10	1402 ± 9
K100	Muscovite schist	Monazite	Hypidioblast		15-20	1403± 15	
Metamorphic M II							
K89	Muscovite schist	Monazite	Skeletal poikiloblast	>300	~0.6	1379 ± 27	
K96	Muscovite schist	Monazite	Skeletal poikiloblast	>300	~0.6	1374 ± 13	1375 ± 8
K100	Muscovite schist	Monazite	Skeletal poikiloblast	>300	0.5-1	1375 ± 15	
Metamorphic M III							
K101	Banded pelite	Monazite	Hypidioblast/ xenoblast	Up to 100	0.8-2	991 ± 16	991 ± 16

Note:

*Weighted mean $^{207}Pb/^{206}Pb$ age (95% confidence level) of individual samples.

[†]Combined mean age (95% confidence level) calculated for each group.
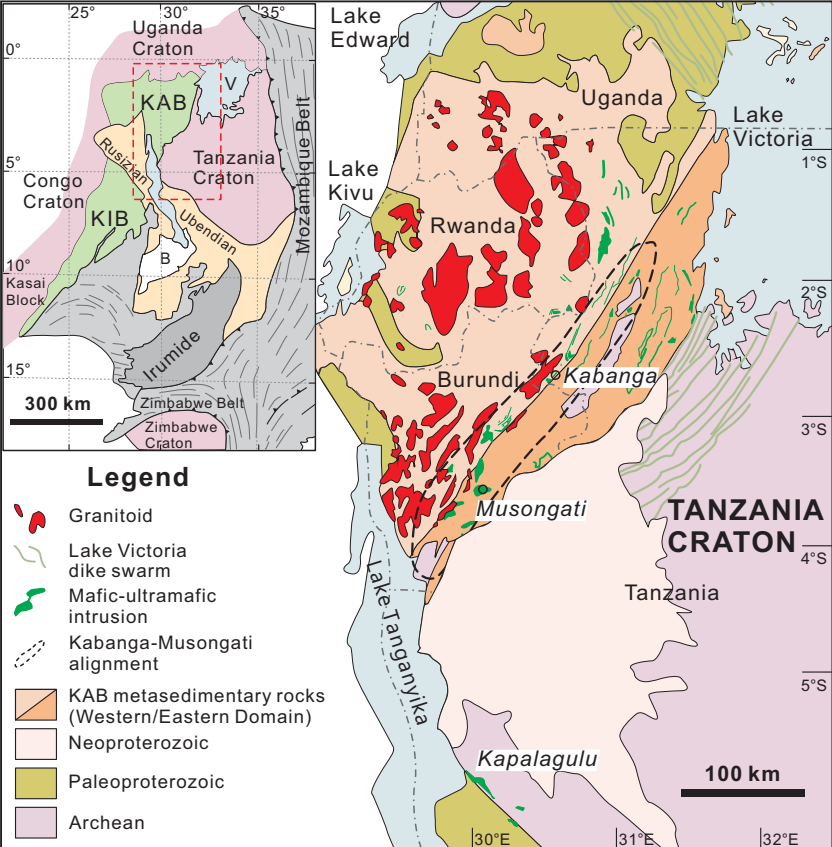
Figure 1
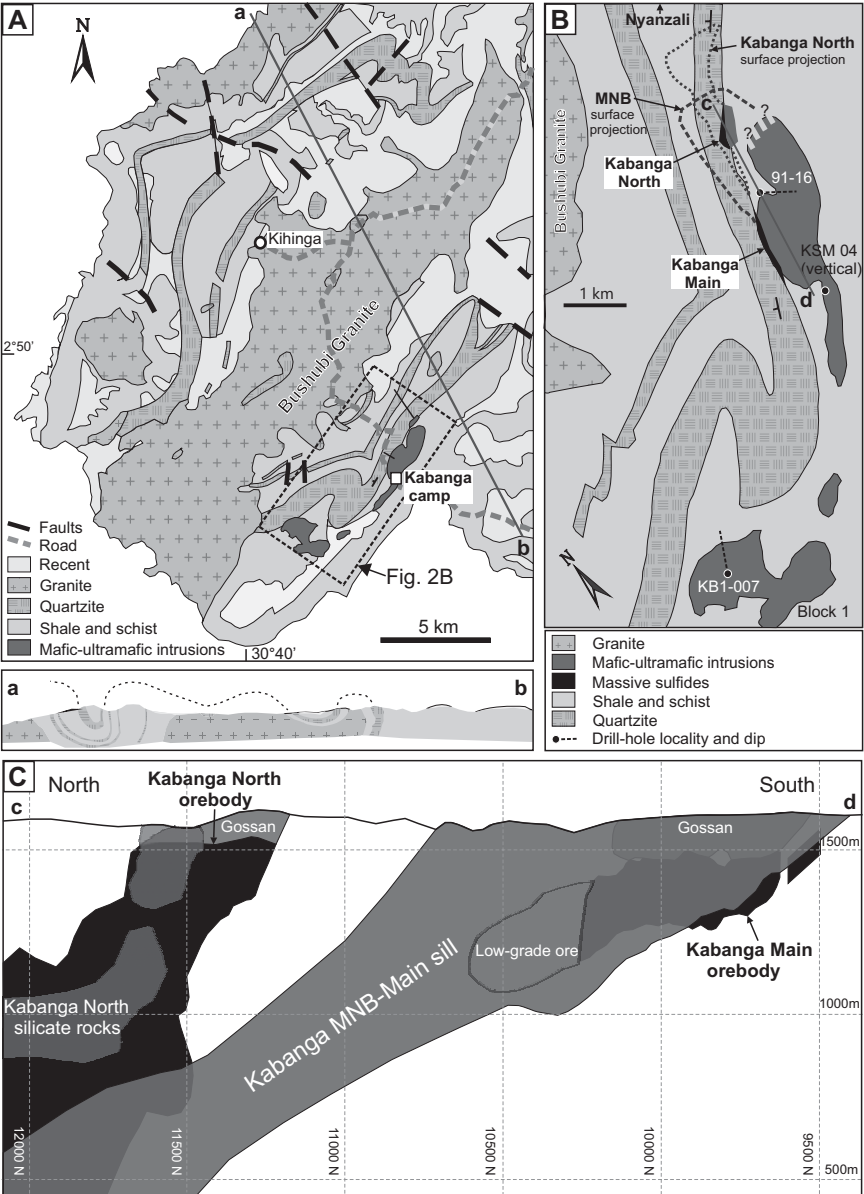
Figure 2

Figure 3

Figure 4

A. K99 (0911D) — 1398 ± 10 Ma

B. K99 (0911K) — 1378 ± 5 Ma

C. K100 (0911A) — A.1-1: 1379 ± 8 Ma; A.1-2: 1394 ± 12 Ma

D. K100 (0911M) — 1376 ± 36 Ma; 1350 ± 38 Ma; 1302 ± 39 Ma; 1267 ± 35 Ma
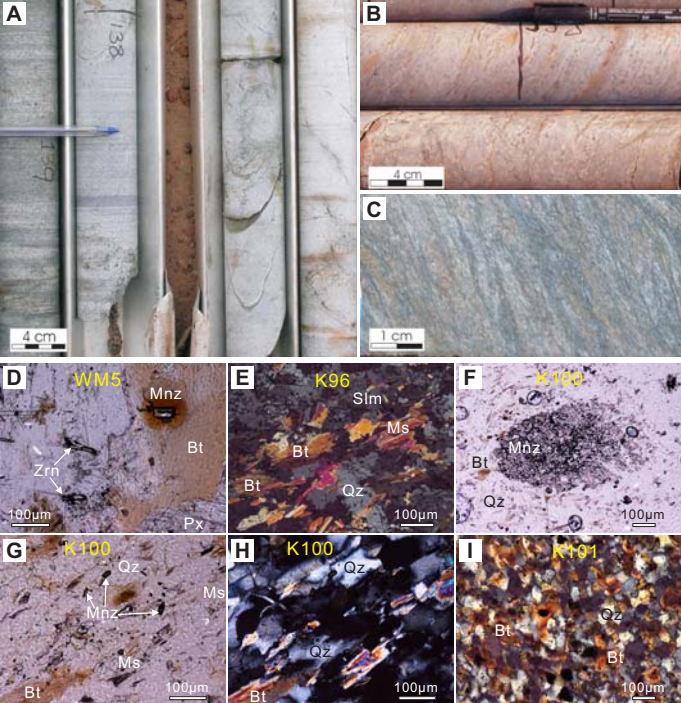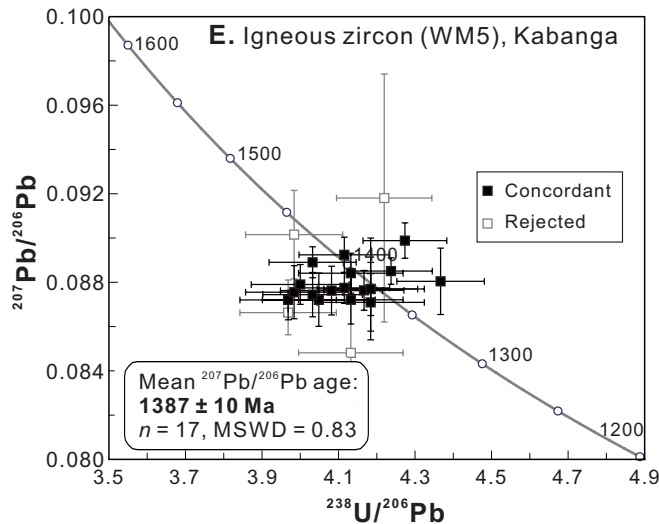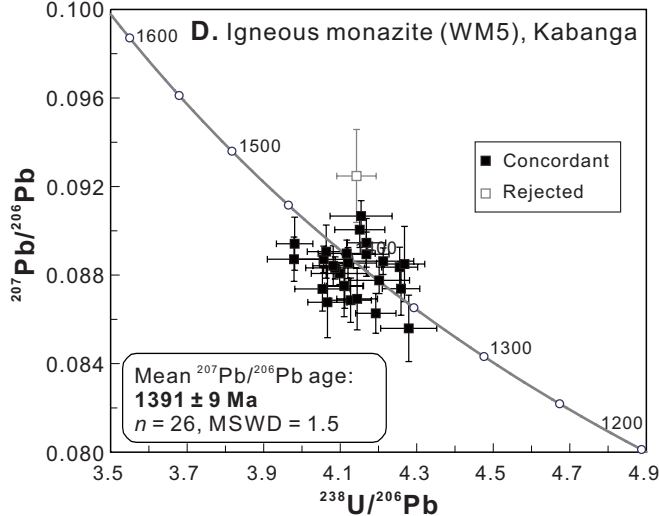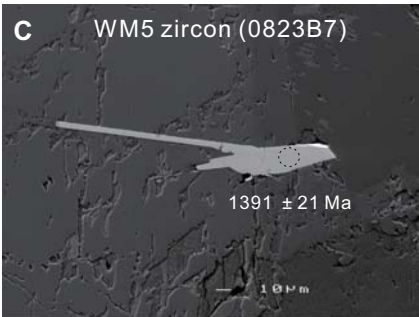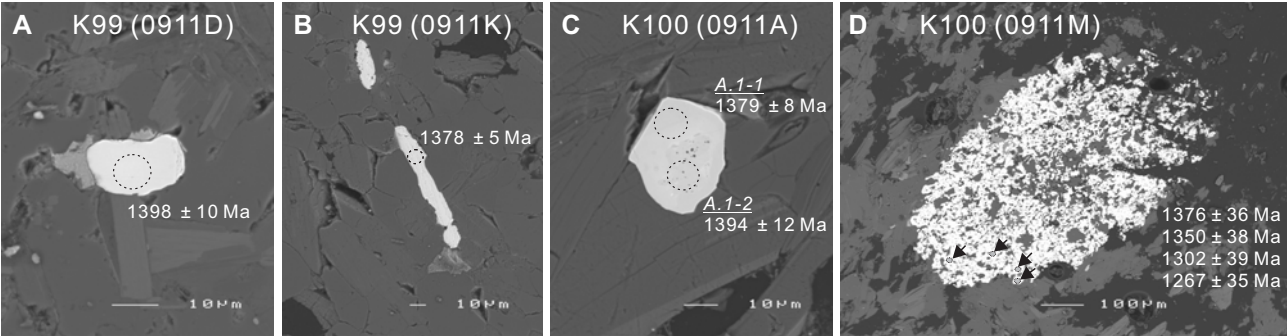
E. Monazite in muscovite schist (K99 & K100)

data point error symbols are 1 σ

K99
Mean $^{207}Pb/^{206}Pb$ age: **1401 ± 10 Ma**
$n = 4$, MSWD = 0.12

K100
Mean $^{207}Pb/^{206}Pb$ age: **1403 ± 15 Ma**
$n = 4$, MSWD = 0.64

K99 & K100 high-Th
Mean $^{207}Pb/^{206}Pb$ age: **1402 ± 9 Ma**
$n = 8$, MSWD = 0.33

K100 low-Th + rim
Mean $^{207}Pb/^{206}Pb$ age: **1375 ± 15 Ma**
$n = 4$, MSWD = 1.08

M-I monazite
M-II monazite
Rejected
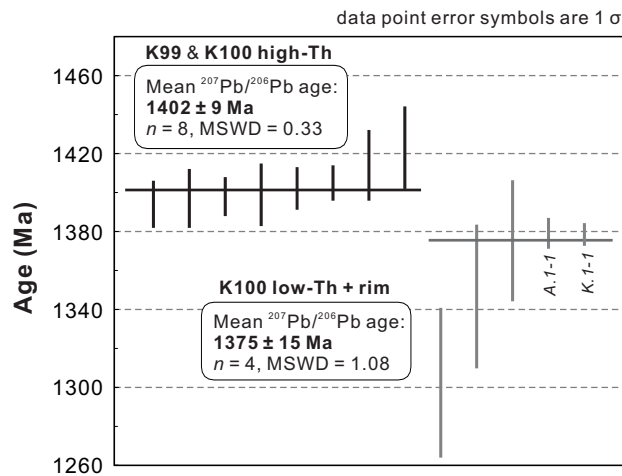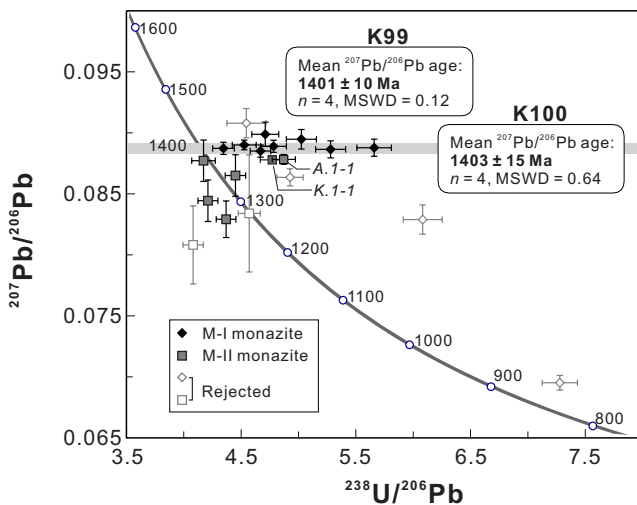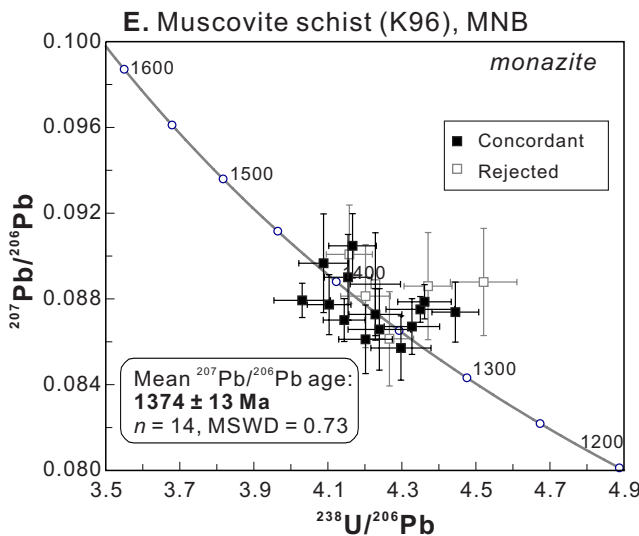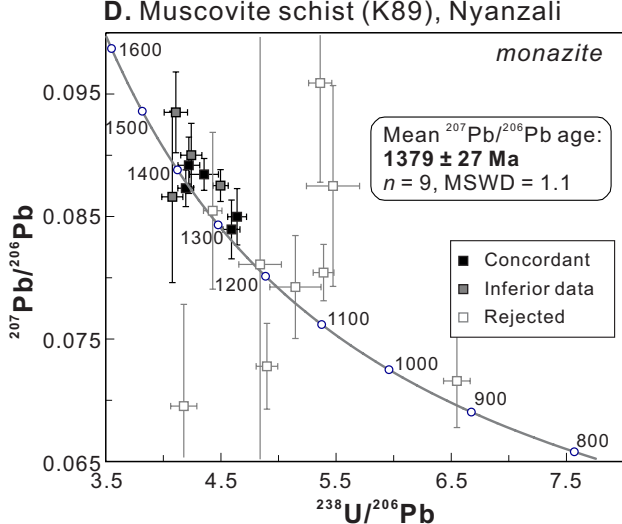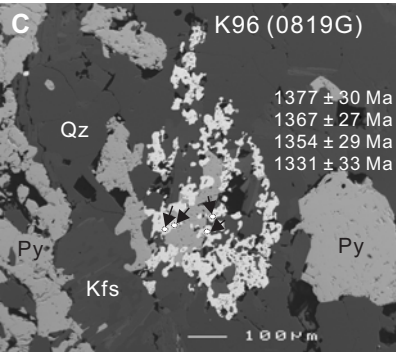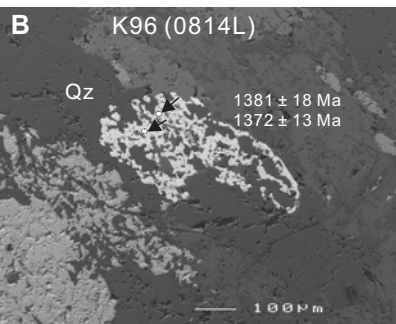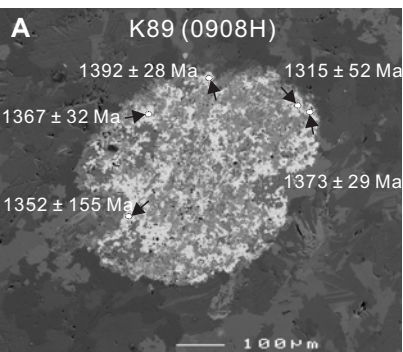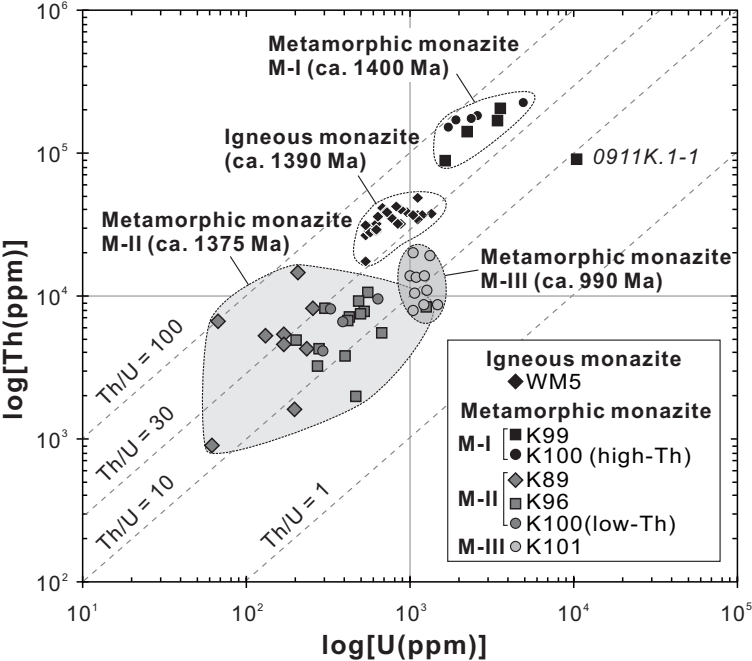
Figure 5

Figure 6

Figure 7
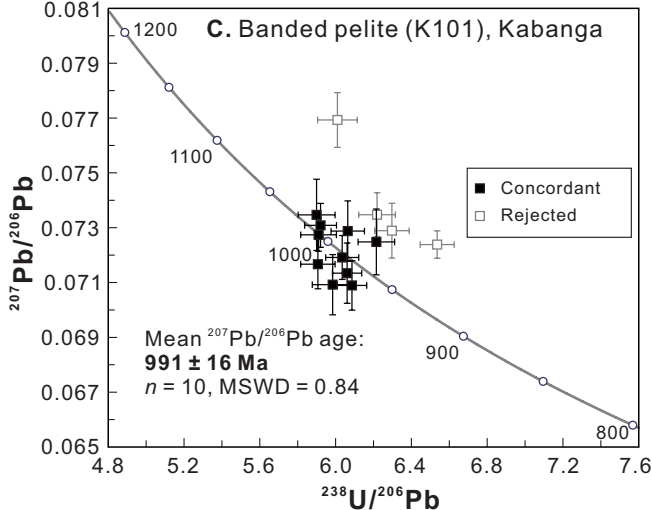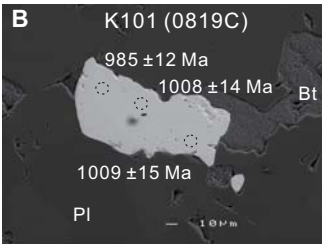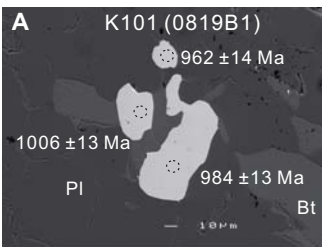
Figure 8

Figure 9

Figure 10